



# Electro-optic tunable grating-assisted optical waveguide directional coupler in lithium niobate

Jun Hui Li<sup>1</sup> · Kai Xin Chen<sup>1</sup>

Received: 13 November 2022 / Accepted: 3 February 2023 / Published online: 13 February 2023  
© The Author(s), under exclusive licence to Springer-Verlag GmbH Germany, part of Springer Nature 2023

## Abstract

In this paper, a high-performance electro-optical tunable grating-assisted directional coupler (GADC) is proposed and demonstrated experimentally. Our proposed GADC consists of a two-mode waveguide (TMW) and a single-mode waveguide (SMW) formed with lithium niobate (LN). By introducing a long-period waveguide grating into the side-wall of the TMW to compensate for the phase mismatch of the fundamental modes of the SMW and TMW, the fundamental modes of the two waveguides can be coupled efficiently each other at a specific wavelength. Furthermore, push–pull electrode structure is introduced to achieve the electro-optic (EO) tuning function featuring high speed, low driving voltage, and large tuning range. The best LN GADC we fabricated on x-cut LN substrate using annealing proton exchange process shows a high isolation of ~34 dB at 1532.9 nm wavelength, quite large EO tuning efficiency of 1.195 nm/V (1526.4–1549.1 nm) or 1.736 nm/V (1576.1–1602.2 nm), and a thermo-optic tuning efficiency of 0.128 nm/°C (22–60 °C). Our proposed LN GADC can find applications in the fields of high-speed tunable wavelength filtering, mode filtering, and EO modulation.

## 1 Introduction

Grating-assisted directional coupler (GADC) is an important optical waveguide device because it is capable of achieving efficient coupling between the two modes having mismatched phase [1, 2]. The two same-order modes of the two waveguides with different widths are not synchronized, in another words, are phase mismatched because they have different velocity and momentum due to their different effective refractive indices. This fact leads to that efficient evanescent coupling between the two same-order modes is impossible by employing an asymmetric directional coupler (ADC) because the conservation of momentum cannot be satisfied when one mode is coupled to another, no matter how close the two waveguides are. To solve this phase mismatch issue, it is suggested to introduce a grating into the ADC to compensate the phase mismatch between the two modes so as to achieve efficient mode coupling [2]. According to the

grating type and the propagation direction of the coupled modes, GADC can be divided into Bragg grating-assisted contra-directional couplers [3–16] and long-period gratings (LPG)-assisted co-directional couplers [17–24].

GADC is developed on basis of single-waveguide grating coupler. As early as the 1970s, many researchers such as Paek [25] and Yariv [26, 27] et al. analyzed periodic structures formed on a straight waveguide and developed single-waveguide gratings that can be used as a filter [28] or a reflector in distributed feedback laser [29]. Although the single-waveguide grating can achieve quite narrow bandwidth, the application of this dual port device is relatively narrow. In 1985, Syms proposed a four-ports device combining grating and directional coupler [1], i.e., GADC. GADC provides a new way to improve the performances of the coupler and the grating. Due to its compact structure, easy integration, versatility, and good wavelength selectivity, GADC is now widely used in various scenarios, such as co-directional coupler [3, 4], optical add-drop filter [5–8, 18], polarization splitter [9], microring resonator [10], multimode resonator [11], tunable delay line [12], wavelength division multiplexer [13, 14, 19], mode division multiplexer [15, 16, 23], filter [17, 20, 21], mode filter [22], optical sensing [23], and so on.

Tunability is the key for improving the performance of optical waveguide devices, realizing reconfigurable optical

✉ Kai Xin Chen  
chenkx@uestc.edu.cn

Jun Hui Li  
ljh@std.uestc.edu.cn

<sup>1</sup> School of Optoelectronic Science and Engineering,  
University of Electronic Science and Technology of China,  
Chengdu 611731, China

waveguide devices, and reducing the process requirements in the fabrication of optical waveguide devices. Up to now, the tunability of optical waveguide devices are usually realized based on the electro-optic (EO) and the thermo-optic (TO) effects, where the EO effect includes linear EO effect (i.e., Pockels effect) and plasma dispersion effect. Among them, EO tuning is more fascinating due to its high tuning speed and low power consumption. Nowadays, different types of EO tunable single-waveguide grating have been realized based on different EO materials, such as EO polymer [30], silicon on insulator (SOI) [31], lithium niobate (LN) [32], and hybrid glass waveguide/liquid crystal [33], their low tuning efficiency (usually less than 100 pm/V), however, would limit their practical applications.

Compared with the single-waveguide grating, GADC, a composite structure of the coupler and the grating, has the potential to achieve quite high tuning efficiency. Among the above GADC-type devices, the devices fabricated with SOI adopt plasma dispersion effect [3] or TO effect [7, 12, 14] to achieve the tunability, and the devices fabricated with polymer [6, 23] also adopt TO effect to realize this goal. Although the devices in [20] and [21], fabricated with semiconductor material InGaAsP/InP and EO polymer, respectively, adopt linear EO effect to achieve the tunability, the former has low tuning efficiency due to its small EO coefficient of InP, while the latter has depolarization and stability problems. In comparison with InP and EO polymer, lithium niobate (LN) is the most promising material platform to fabricate these tunable GADC-type devices due to its wide transparent window, large EO coefficient, stable physical and chemical properties, and mature optical waveguide fabrication technology [34, 35]. Therefore, it is of great significance to combine the advantages of LN crystal and GADC structure to develop GADC-type devices that have stable performance, low loss, and high tuning efficiency.

Previously, we have realized asymmetric directional coupler [36] and cascaded three-dimensional directional coupler [37] in LN. The former can realize efficient and tunable coupling between the  $E_{11S}$  mode in single-mode waveguide (SMW) and the  $E_{21T}$  mode in two-mode waveguide (TMW) and, hence, switchable mode multiplexing; and the latter further realizes the switchable mode (de)multiplexing functions for the  $E_{11}$ ,  $E_{21}$ , and  $E_{12}$  modes by cascading two asymmetric directional couplers. In addition, we have also successfully developed the GADC-type mode filter based on LN material to meet the needs of some special application scenarios where the fundamental  $E_{11T}$  mode in TMW needs to be filtered [22]. Our previous GADC-type mode filter achieved an isolation of 29 dB at the wavelength of 1551.7 nm. However, its EO tuning efficiency is low (only 0.182 nm/V) because only one coupled waveguide is tuned. To improve the EO tuning efficiency of LN optical waveguide GADC, in this paper, we further introduce and

fabricate successfully a set of push–pull electrode to tune the two coupled waveguides. We also improve the waveguide fabrication process to reduce the propagation loss. With these innovations, we designed and fabricated dozens of GADCs with somewhat different periods on a single x-cut LN chip using annealing proton exchange (APE) process, the best one of them shows maximum isolations of ~34 dB (1532.9 nm) and ~29 dB (1533.1 nm) for the TMW and SMW channels, respectively. We further package the best one and investigate its EO tuning and modulation features as well as TO tuning feature, which gives an EO tuning efficiency of 1.195 nm/V (1526.4–1549.1 nm) or 1.736 nm/V (1576.1–1602.2 nm), and a thermo-optic tuning efficiency of 0.128 nm/°C (22–60 °C). At least six times enhancement of EO tuning efficiency is achieved compared with our previous result. Our proposed LN GADC can find applications in the fields of high-speed tunable wavelength filtering, mode filtering, and EO modulation.

## 2 Device structure and design

As shown in Fig. 1a, our proposed LN GADC consists of an asymmetric directional coupler (ADC), an LPG, and a set of push–pull electrode. The ADC is composed of an SMW and a TMW with a spacing of  $S$ . The LPG is formed on the inner side of the TMW. In this work, these optical waveguides and the LPG are formed with APE process simultaneously. To employ the maximum EO coefficient  $\gamma_{33}$  of LN, the x-cut LN wafer and y-propagation layout are adopted. Because the LN waveguides formed with APE process support only the light wave whose electric field is along  $z$  direction [35], the SMW here only supports the fundamental mode  $E_{11S}$  polarized along the  $z$  direction, while the TMW only supports the fundamental mode  $E_{11T}$  and the first-order mode  $E_{21T}$ , both polarized along the  $z$  direction. The chromium gold electrodes are placed between the SMW and TMW and both sides of the two waveguides, as shown in Fig. 1. Such an electrode structure can utilize the opposite electric field in the SMW and TMW to realize the push–pull tuning function and, hence, reduce the tuning voltage and improve the tuning efficiency. In addition, to avoid the light absorption induced by the metal electrode, a silicon dioxide ( $\text{SiO}_2$ ) buffer layer is formed on the LN waveguides to isolate the waveguides from the electrodes, as shown in Fig. 1b. Obviously, if the widths of the SMW and the TMW are quite different, the propagation constants of the  $E_{11S}$  and  $E_{11T}$  modes in the two waveguides are also quite different; thus, the coupling between the  $E_{11S}$  and  $E_{11T}$  modes is impossible. However, the introduction of the LPG can compensate for the difference of the propagation constants of the two fundamental  $E_{11S}$  and  $E_{11T}$  modes so as to realize efficient mode coupling based on phase matching.

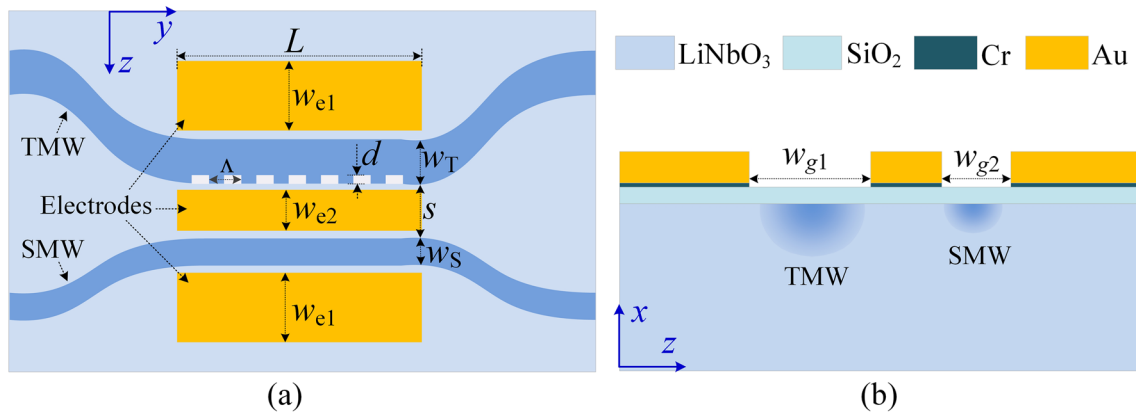


**Fig. 1** a Schematic diagrams showing a the top view of the proposed GADC and b cross-sectional view of the coupling region of the proposed GADC

To design the proposed GADC, we need to know the effective refractive indices of the  $E_{11S}$  and  $E_{11T}$  modes, determined by the width of the SMW and the TMW. For this purpose, we fabricated many sets of trial LN waveguides with different widths through the APE process. Each set of waveguides includes ten optical waveguides with the same width so as to measure the effective refractive index of the waveguide easily [36, 38]. Different from our previous work [22, 36], here, we used the mixed solution of benzoic acid and lithium benzoate for proton exchange. We fabricated several groups of optical waveguides with widths of 5–7  $\mu\text{m}$  and 10–13  $\mu\text{m}$  (step size 0.5  $\mu\text{m}$ ) using the same exchange temperature of 250  $^\circ\text{C}$  and annealing temperatures of 350  $^\circ\text{C}$ , but slightly different exchange and annealing times. We then measured the effective refractive index of these waveguides at the wavelength of 1538.3 nm with prism-coupler system (Metricron, Model 2010. The nominal uncertainty is  $\pm 0.0003$ ). According to the measured results, after exchange of 4.0 h and annealing of 3.6 h, the effective refractive index  $N_{11S}$  of the  $E_{11S}$  mode in a 6.0- $\mu\text{m}$ -width SMW is 2.14114, while the effective refractive indices  $N_{11T}$  and  $N_{21T}$  of the  $E_{11T}$  and  $E_{21T}$  modes in a 10.0- $\mu\text{m}$ -width TMW are 2.14320 and 2.13950, respectively. Obviously, the effective refractive indices of these three modes are quite different, which means the phase-matching mode coupling between them can be avoided. Therefore, the width  $w_s$  of the SMW is set to 6.0  $\mu\text{m}$ . Further, considering the impact of the grating on the modes of the TMW, the width of the TMW should be  $(10 + d/2)$   $\mu\text{m}$  [39]. At the same time, considering that the LPG is also fabricated simultaneously with the waveguide through the APE process, its refractive index contrast is small. Thus, to increase the coupling efficiency and reduce the difficulty of the grating fabrication but not to increase the propagation loss of the waveguide,

the grating depth  $d$  is set to 1.2  $\mu\text{m}$ , about one-tenth of the width of the TMW. Based on the above analysis, the width  $w_t$  of the TMW is set to 10.6  $\mu\text{m}$ .

The period  $\Lambda$  of the grating can be calculated using the formula [19]:

$$\Lambda = \frac{\lambda_0}{N_{11T} - N_{11S}} = \frac{\lambda_0}{\Delta N_{11}} \tag{1}$$

with the measured  $N_{11T}$  and  $N_{11S}$  in our trial, the calculated  $\Lambda$  is 752.4  $\mu\text{m}$  at the resonant wavelength of 1550 nm. To place the tuning electrode between the SMW and TMW but not to increase the length of the device significantly, a moderate space  $S$  of 4.0  $\mu\text{m}$  between the two waveguides is chosen. Finally, with the above parameters, the grating length of 13,572  $\mu\text{m}$ , corresponding to 18 grating periods, is obtained using the beam propagation method (Rsoft BPM) to simulate the light propagation through the grating when the grating duty cycle is set to 50%, which just like we did in our previous work [22]. Figure 2a, b presents the simulated propagation dynamics when the z-polarized  $E_{11}$  mode at 1550 nm was launched into the SMW and the TMW of the designed GADC, respectively, which clearly show efficient coupling between the  $E_{11S}$  mode and the  $E_{11T}$  mode. While Fig. 2c presents the simulated propagation dynamics when the z-polarized  $E_{21}$  mode at 1550 nm was launched into the TMW of the designed GADC, which shows that the excited  $E_{21T}$  mode almost stays in the TMW and there is almost no mode coupling between the SMW and the TMW.

A simple lumped tuning electrode structure is adopted in this work. According to the waveguide structure shown in Fig. 1 and the above waveguide parameters, the central electrode width  $w_{e2}$  is set to 4  $\mu\text{m}$ . The electrode width  $w_{e2}$  on both sides is set to 30  $\mu\text{m}$ . The electrode spacing  $w_{g1}$  and  $w_{g2}$  are set to 12  $\mu\text{m}$  and 8  $\mu\text{m}$ , respectively. The electrode length is 13.95 mm.

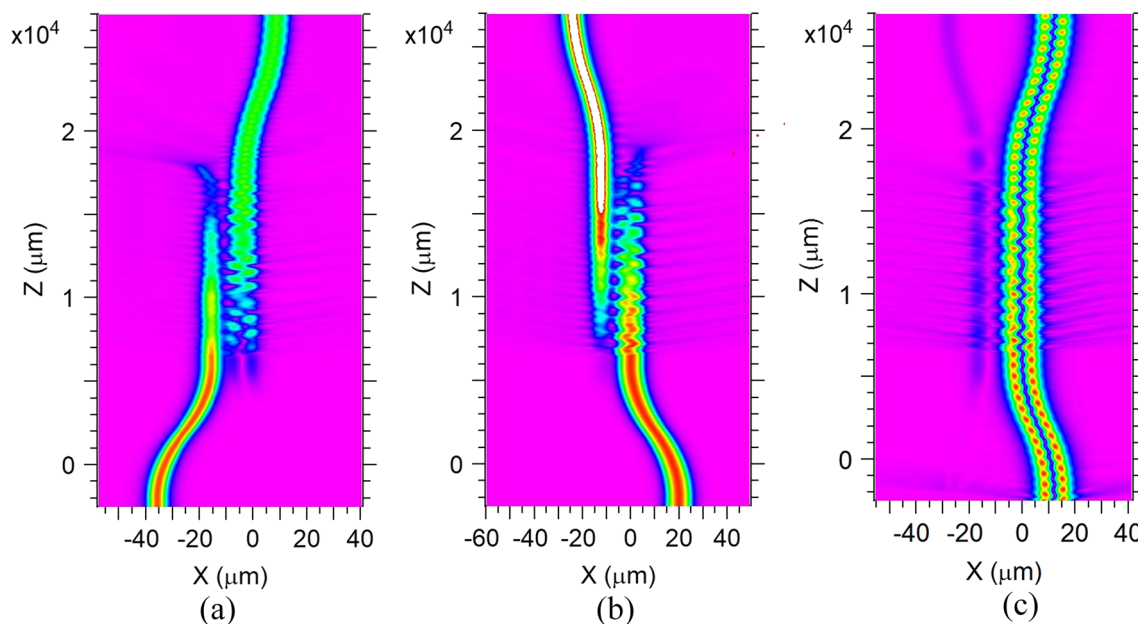


**Fig. 2** Simulated propagation dynamics when the z-polarized  $E_{11}$  mode at 1550 nm was launched into **a** the SMW and **b** the TMW of the designed GADC, respectively. **c** Simulated propagation dynamic

when the z-polarized  $E_{21}$  mode at 1550 nm was launched into the TMW of the designed GADC

### 3 Device fabrication

We fabricate the proposed GADC using standard photolithography and APE process as we used to fabricate the trial waveguides. The fabrication process is outlined below. A layer of  $\text{SiO}_2$  used as the mask layer during exchange was grown on the clean x-cut LN wafer by plasma enhanced chemical vapor deposition (PECVD). Then the device pattern was defined on the photoresist layer by photolithography and transferred subsequently to the  $\text{SiO}_2$  layer through wet etching. After the residual photoresist was removed, the patterned LN substrate was submerged in the mixed solution of benzoic acid and lithium benzoate for proton exchange. Next, the exchanged LN substrate was annealed to reduce the waveguide loss and restore its EO activity. The exchange and annealing parameters are the same as the optimal parameters used in the fabrication of the above trial waveguide, i.e., the samples were exchanged at 250 °C for 4 h, and then annealed at 350 °C for 3.6 h. After that, we cut the chip and polished its two end faces to obtain the input/output interface, where each end face has an angle of 8° with respect to the z direction so as to prevent the light reflected back into the waveguide. The total length of the chip after polishing is ~25 mm. Finally, we fabricated successfully a set of push-pull chromium gold electrode with a thickness of about 1  $\mu\text{m}$  and a length of 13.95 mm through electron beam evaporation, lithography with high-precision alignment, and electroplating processes. Here, to reduce the light absorption loss induced by the metal electrode, a layer of

about 130-nm-thick  $\text{SiO}_2$  used as a buffer layer was grown on the surface of the waveguide by PECVD before fabricating the electrode. In view of the high sensitivity of the resonant wavelength of LPG to the grating period and the errors in the design and fabrication process, we designed and fabricated dozens of GADCs with somewhat different periods on a single LN chip, as shown in Fig. 3a. Figure 3b shows a microscope photograph of the fabricated tuning electrode, indicating that the fabrication of the electrode is quite successful.

### 4 Device measurement

We first investigated the transmission of our fabricated LN GADC at room temperature of 22 °C. Broadband light signal from an amplified spontaneous emission (ASE) light source (B&A technology AS4600) was launched into the TMW or SMW of the GADC through a standard single-mode polarization maintaining fiber (SMPMF). To excite only the  $E_{11S}$  or  $E_{11T}$  mode polarized along z direction in the SMW or TMW, we adjusted the SMPMF carefully so as to launch the light exactly at the center of the input waveguide. The light output from the SMW or TMW was collected by a single-mode fiber (SMF) and monitored by an optical spectrum analyzer (OSA) (YOKOGAWA, AQ6375B). The measurements for multiple GADCs show that the GADC with a period of 754  $\mu\text{m}$  (denoted as GADC754) has the best performance. Figure 4a, b shows the normalized transmission



**Fig. 3** **a** Photograph of our typical fabricated chip including dozens of GADC devices and **b** a microscope photograph of the fabricated tuning electrode

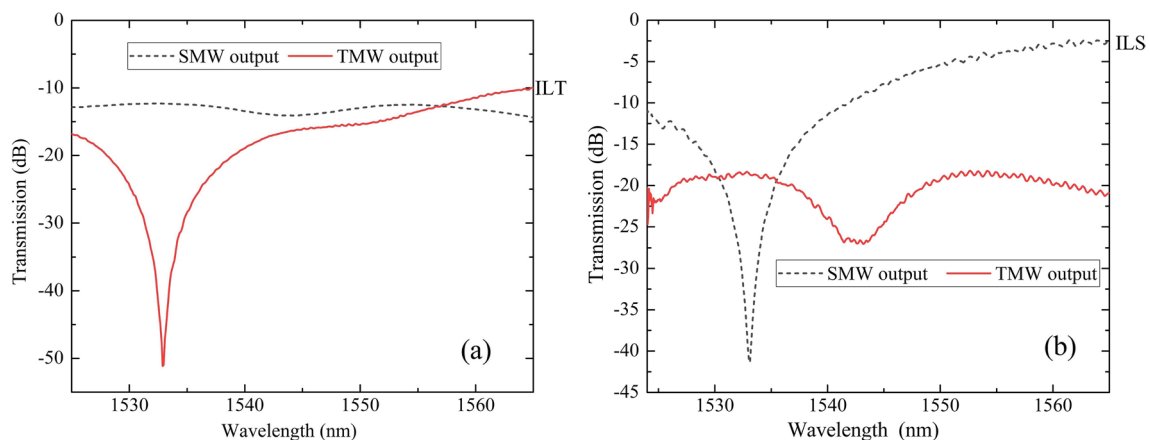
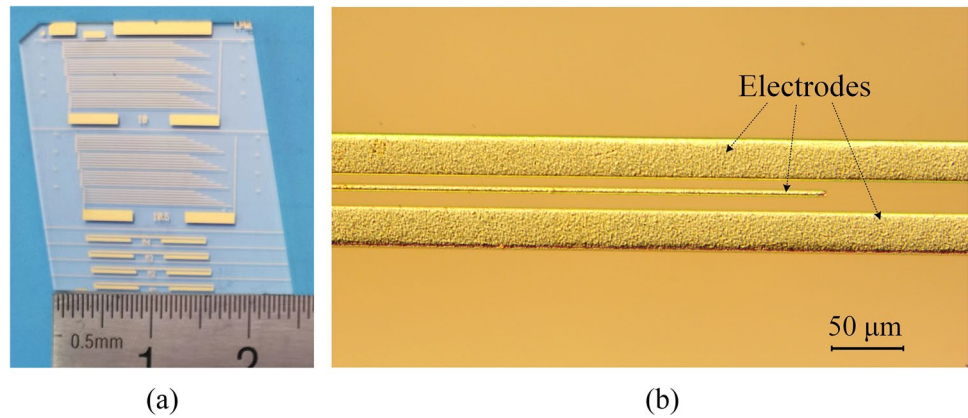


**Fig. 4** Normalized transmission spectra from the TMW and the SMW of GADC754 measured with broadband light launched into **a** the TMW and **b** the SMW

of GADC754 when the broadband light signal was launched into the TMW and SMW of GADC754, respectively, where the normalization was done with respect to the spectrum of fiber to fiber. It can be seen from Fig. 4a that, when the light is input from the TMW, the transmission spectrum of the TMW exhibits a distinct rejection band with a maximum contrast of  $\sim 34$  dB at the center wavelength 1532.9 nm, while the output spectrum of the SMW exhibits somewhat complementary pass band. This indicates that the  $E_{11T}$  mode of the TMW is coupled into the  $E_{11S}$  mode of the SMW near the rejection band. In addition, from Fig. 4b, it can be inferred that when the light is input from the SMW, the output spectrum of the SMW exhibits a distinct rejection band with an isolation of  $\sim 29$  dB at the wavelength of 1533.1 nm, while the spectrum output from the TMW exhibits a distinct complementary pass band near the rejection band, indicating an efficient coupling from the  $E_{11S}$  mode of the SMW to the  $E_{11T}$  mode of the TMW.

According to the normalized transmission spectrum shown in Fig. 4a, b, the minimum insertion losses of the

TMW and SMW of GADC754 are  $\sim 10.0$  dB (denoted as ILT, see Fig. 4a at 1565 nm) and  $\sim 2.5$  dB (denoted as ILS, see Fig. 4b at 1565 nm). As a comparison, we also measured the insertion losses of a few straight reference waveguides fabricated simultaneously on our GADC chip using the same parameters as the SMW and the TMW (also with 18 grating periods). For the fundamental modes (the  $E_{11S}$  and  $E_{11T}$  mode), the measured insertion losses of the reference TMW and SMW are 2.5 dB and 2.2 dB, respectively. The coupling losses between the fiber and the TMW and the SMW are estimated to be with a same value of  $\sim 0.5$  dB/facet. Correspondingly, the propagation losses of the TMW and the SMW are  $\sim 0.58$  dB/cm and 0.48 dB/cm. Here, the relatively large insertion loss of the TMW of GADC754 can be mainly attributed to more overlap between the metal electrode and the TMW, which induces a significant absorption loss. Although the metal absorption loss can be reduced by increasing the thickness of  $\text{SiO}_2$  buffer layer, it will lead to the decrease of EO tuning

efficiency. Thus, there should be a trade-off between the metal absorption loss and the EO tuning efficiency.

In addition, if we assume that the light travels the same lengths in the TMW and the SMW no matter which waveguide it is input from, then according to the above insertion losses of the TMW and the SMW of GADC754, the normalized output from the SMW and the TMW should be with the same value of  $\sim -6.25$  dB ( $= IL_{T/2} + IL_{S/2} = 5.0$  dB + 1.25 dB) at the resonance wavelength (the flatness of the ASE light source is better than 1 dB). However, from Fig. 4a, the output from the SMW is only  $-12.5$  dB at 1532.9 nm, which means there exists a coupling loss of  $\sim 6.25$  dB when the  $E_{11T}$  mode is coupled to the  $E_{11S}$  mode. Similarly, from Fig. 4b, the output from the TMW is only  $-18$  dB at 1533.1 nm, which also means there exists a coupling loss of  $\sim 11.75$  dB when the  $E_{11S}$  mode is coupled to the  $E_{11T}$  mode. The two coupling losses can be attributed to the absorption induced by the middle metal electrode between the two waveguides, which is also the reason that the measured transmission spectra shown in Fig. 4a, b do not show obviously complementary feature at the resonance wavelength of 1532.9 nm and 1533.1 nm. At last, apart from the above absorption losses and after ignoring the above propagation and the butt coupling losses, the coupling efficiencies of the two cases can be calculated approximately using the normalized power at 1532.9 nm and 1533.1 nm shown in Fig. 4a, b, and the calculated results are larger than 99% at these two resonance wavelengths.

To confirm that the rejection band in Fig. 4a, b is caused by the light coupling, we further investigated the light coupling using a tunable laser (OPEAK DFB-C-WTx) as the light source to excite  $E_{11T}$  mode in the TMW, and then took the near-field images of the output light from the SMW and

TMW with an infrared camera (Micron Viewer 7290A). The captured images over the wavelength range 1530–1540 nm are shown in Fig. 5a. At the resonance wavelength of 1532.9 nm, a complete coupling between the  $E_{11T}$  and the  $E_{11S}$  mode is achieved, while at other wavelengths, only part of the  $E_{11T}$  mode is coupled to the  $E_{11S}$  mode. The above mode coupling characteristics are completely consistent with the results shown in Fig. 4a, indicating that the rejection band in the transmission of the TMW is caused by the coupling between the  $E_{11T}$  and  $E_{11S}$  modes.

Additionally, we also investigated the transmission of the  $E_{21T}$  mode in the TMW. We adjusted the input SMPMF carefully to introduce a suitable offset between the two central axes of the fiber and the waveguide so as to excite  $E_{21T}$  mode in the TMW. The photo in the red box at the bottom-right corner of Fig. 5 shows the near-field image captured at the wavelength of 1532.9 nm at the output end of GADC754. As expected, there is no mode coupling between the  $E_{21T}$  and  $E_{11S}$  modes, which means our proposed device can filter  $E_{11S}$  mode but would not affect the transmission of the  $E_{21T}$  mode.

To facilitate the investigation of the EO and TO tunability of the device, we further packaged GADC754 unit on the chip. The process is as follows: first, we cut off the parts with poor performance from the LN GADC chip; second, the two ends of the TMW and the SMW of GADC754 were pigtailed with an SMPMF array (with two fibers) and an SMF array (with two fibers) using UV glue and subsequent high-temperature aging process, respectively; finally, the chip was placed in a simple packaging box and the device electrode pads were bonded with gold wire to the pin of the packaging box. The photograph of the packaged GADC chip is shown in Fig. 6.

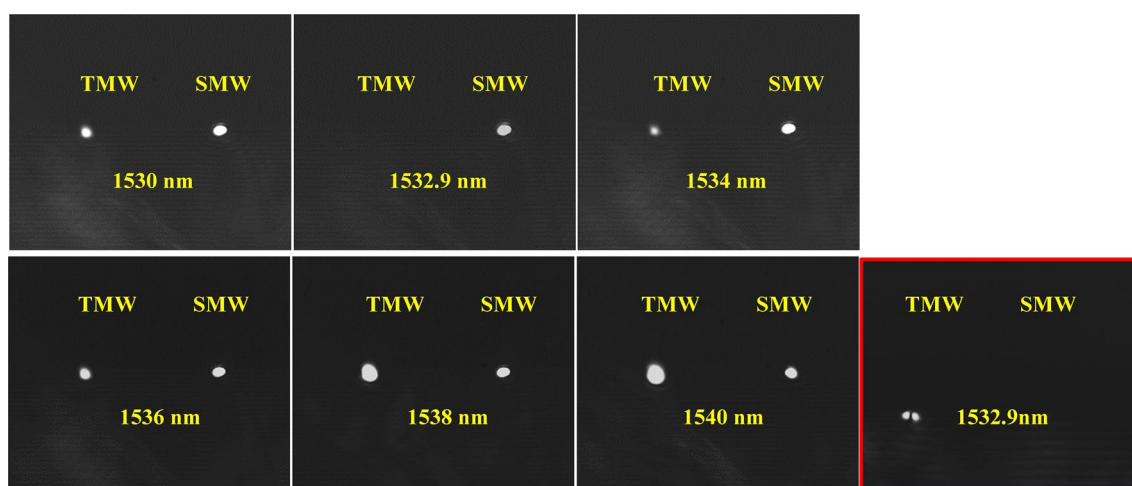
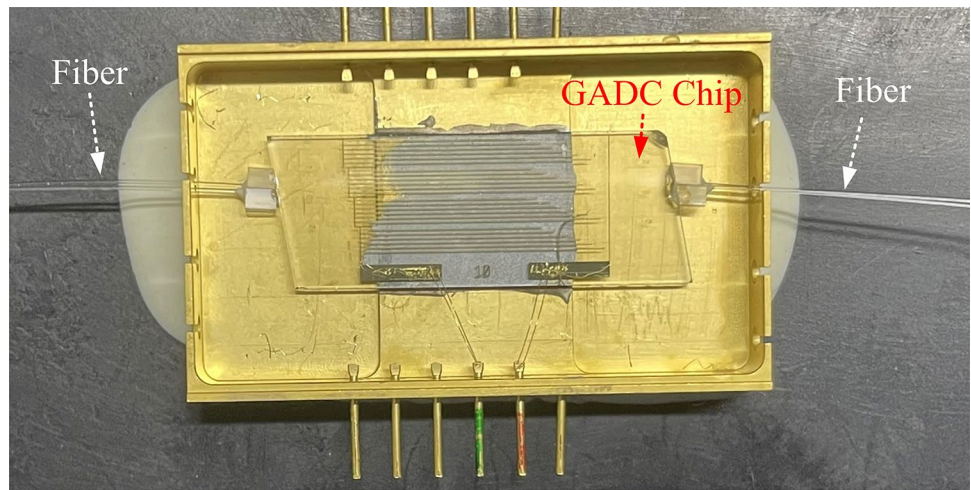


**Fig. 5** Output near-field patterns taken at the output of the TMW and the SMW of GADC754 when the  $E_{11T}$  mode at different wavelengths is excited at the input of the TMW, the pattern in the red box

at the bottom-right corner corresponds to the  $E_{21T}$  mode at 1532.9 nm excited at the input of the TMW

**Fig. 6** A photograph of the packaged GADC chip



We then investigated the EO tuning feature of the packaged GADC754 chip with the above ASE light source and OSA by applying different positive or negative tuning voltages to the electrodes, where a positive (negative) voltage means that the voltage between the side electrodes and the middle electrode is positive (negative). The normalized transmission spectra are shown in Fig. 7a–e. Compared with the measured result before package, which is shown in Fig. 4a, the central wavelength of the transmission spectrum

of the TMW channel shifts from 1532.9 nm to 1533.4 nm after package, a slight change of ~0.5 nm.

As shown in Fig. 7a, when the tuning voltage increases from 0 to 6 V, the central wavelength of the rejection band of the TMW transmission spectrum redshifts from 1533.4 to 1541.04 nm, the isolation drops from 33 to 21 dB, and the insertion loss increases by ~6 dB. Subsequently, as the tuning voltage further increases to 10 V, the central wavelength also further redshifts to 1547.0 nm and the isolation

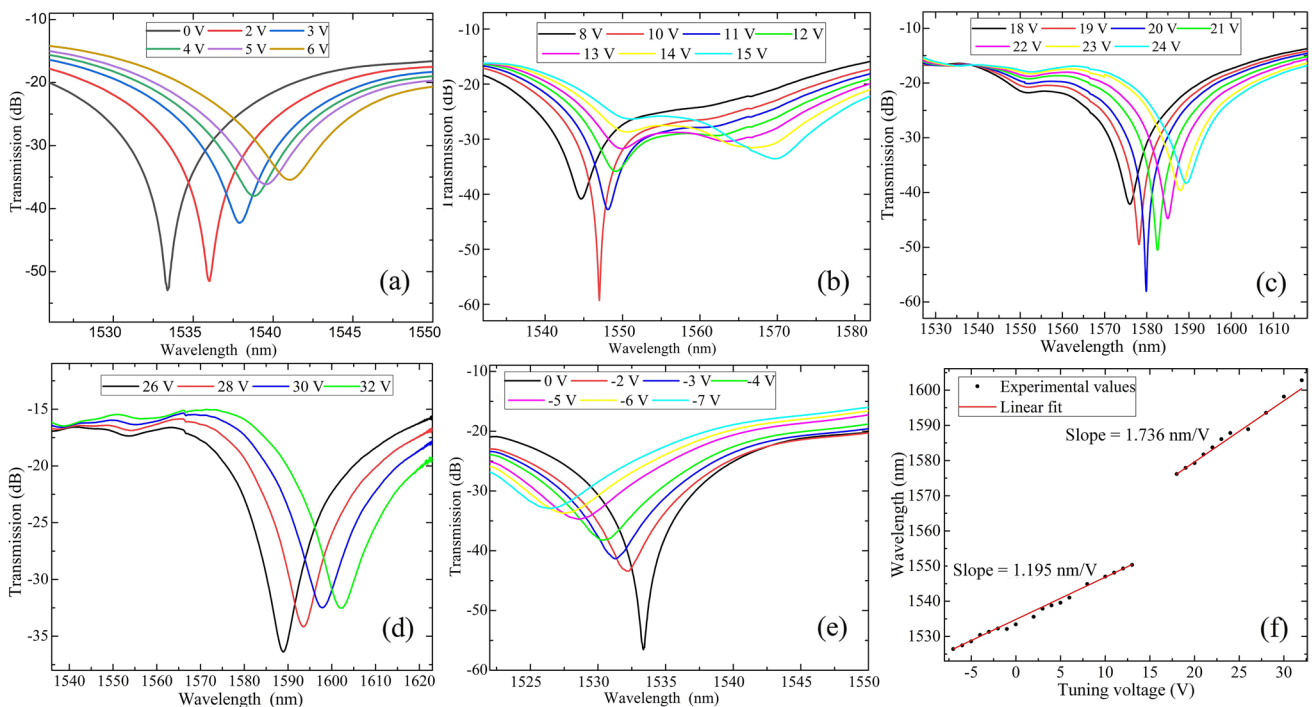


**Fig. 7** Normalized transmission spectra of the TMW channel of the packaged GADC754 measured at different tuning voltages, **a** 0–6 V, **b** 8–15 V, **c** 18–24 V, **d** 26–32 V, **e** 0 to –7 V, and **f** variation of the

center wavelength with the tuning voltage together with the linear fitting lines for the two rejection bands

increases to 44 dB. After that, as the tuning voltage continues to increase, the center wavelength continues to redshift, but the isolation becomes smaller and smaller, and finally almost disappears at the tuning voltage of 15 V, as shown in Fig. 7b. Meanwhile, when the tuning voltage is 12 V, a new rejection band is generated near the wavelength of 1562 nm. This new rejection band has the same EO tuning characteristics as the previous rejection band, its center wavelength redshifts from 1576.1 to 1602.2 nm when the tuning voltage increases from 18 to 32 V, as shown in Fig. 7c, d. The minimum insertion loss is 15 dB while the maximum isolation is 42 dB (corresponding to the tuning voltage of 20 V and the center wavelength of 1579.8 nm), and the isolation is greater than 17.5 dB over the tuning range of 26 nm. Moreover, it can be deduced from Fig. 7d that the tuning range can be further extended toward longer wavelength, but limited by the measurement equipment, no corresponding experimental results are presented here. Additionally, as shown in Fig. 7e, when the applied tuning voltage increases from 0 to  $-7$  V, the center wavelength blueshifts from 1533.4 to 1526.4 nm and the isolation decreases from 36.0 to 6.0 dB.

The above results indicate that GADC754 has two rejection bands, and the two rejection bands overlap partially when the tuning voltage is in the range of 12–15 V, as shown in Fig. 7b, which greatly increases the bandwidth of the device. With the increase of the tuning voltage, the isolation of the first rejection band decreases while the isolation of the second rejection band increases, and the isolation of the two rejection bands are almost the same when the voltage is 13 V. The variation of the central wavelengths of the two rejection bands with the tuning voltage together with the linear fitting lines is shown in Fig. 7f. Linear fitting lines show that the tuning efficiencies are 1.195 nm/V (1526.4–1549.1 nm) and 1.736 nm/V (1576.1–1602.2 nm), respectively. In view of the fact that,

for any GADC, high-efficiency coupling requires not only the perfect phase match condition presented in Eq. (1) but also a suitable coupling length (i.e., grating length), all of these EO tuning feature can be explained as follows. For our fabricated GADC with a fixed grating length, from Eq. (1), the change of  $N_{11T}$  and  $N_{11S}$  due to the EO tuning leads to a corresponding change in  $\lambda_0$ . This is the reason that the rejection band redshifts or blueshifts. However, different  $\lambda_0$  requires different coupling length; therefore, with the change of  $\lambda_0$ , unmatched coupling length results in the decline in coupling efficiency and, hence, the decrease of isolation.

Similarly, we also investigated the EO tuning feature of the SMW channel by launching broadband light signal into the SMW. The normalized transmission spectra measured at different tuning voltage are shown in Fig. 8a. Just like the TMW channel, the central wavelength of the transmission spectrum of the SMW channel has also a shift of  $\sim 1.6$  nm (from 1533.1 to 1534.7 nm) after package, meanwhile the isolation drops from  $\sim 27$  dB to  $\sim 23$  dB. Both changes can be attributed to an imperfect alignment between the fibers and the SMW and the thermal drift caused by the high-temperature aging of the UV glue ( $85^\circ\text{C}$ ). However, they have no any impact on the evaluation of EO tuning of the SMW channel. From Fig. 8a, as the tuning voltage changes from 0 to  $-4$  V, the center wavelength of the rejection band moves from 1534.7 to 1528.4 nm and the isolation reaches its maximum value of 27.0 dB at  $-1$  V. The variation of the center wavelength of the rejection band with the tuning voltage, together with the linear fitting lines, is shown in Fig. 8b, indicating a tuning efficiency of 1.575 nm/V. The above experimental results show that our designed and fabricated LN GADC has large EO tuning range and high tuning efficiency, which makes it a good candidate device for broadband and high-speed tunable wavelength and mode

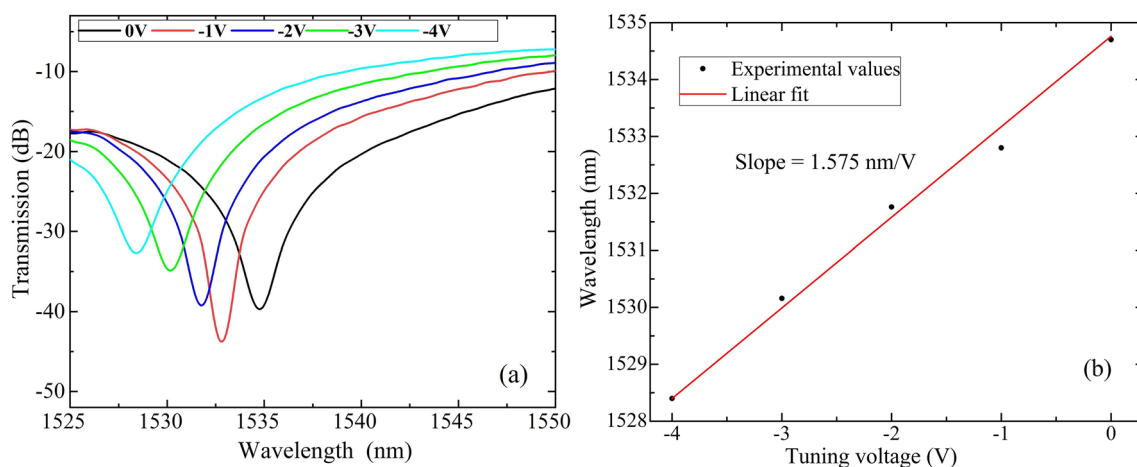


**Fig. 8** **a** Normalized transmission spectra of the SMW channel of GADC754 measured at different tuning voltages from 0 to 4 V and **b** variation of the center wavelength with the tuning voltage together with the linear fitting lines for the rejection band



filter used in the wavelength and mode division multiplexing system.

Further, we investigated EO modulation characteristics of the packaged GADC754. Here, we first determined the optimal operation wavelength by investigating the EO modulation at different operation wavelength from 1530 to 1540 nm when a sinusoidal driving signal at 1 MHz and 6 V (peak to peak) generated by a signal generator (Agilent 33220A) was applied to the tuning electrodes. The modulated light signal output from the TMW was received by the photodetector and sent to the oscilloscope for monitoring. The measured EO modulation at different wavelength is shown in Fig. 9. As expected, the light launched into the GADC can be modulated by the input sinusoidal driving signal and the optimal modulation is achieved at the wavelength of

1533 nm. Subsequently, we selected 1533 nm as the operation wavelength and then investigated the EO modulation of the packaged GADC754 under different sinusoidal driving voltages at 1 MHz. The measured EO modulation is shown in Fig. 10, which shows that the optimal modulation can be achieved at the driving voltage of 6 V. Although the achieved modulation is at low frequency, the proposed GADC structure has potential to achieve a higher-frequency modulation if the coplanar waveguide electrode is used or the proposed GADC is formed with LN thin film, in which a short modulation electrode is possible.

Finally, the TO tuning feature of the packaged GADC754 was also evaluated by investigating the shift of the center wavelength of the rejection band in the TMW transmission spectrum with the change of the ambient temperature. The

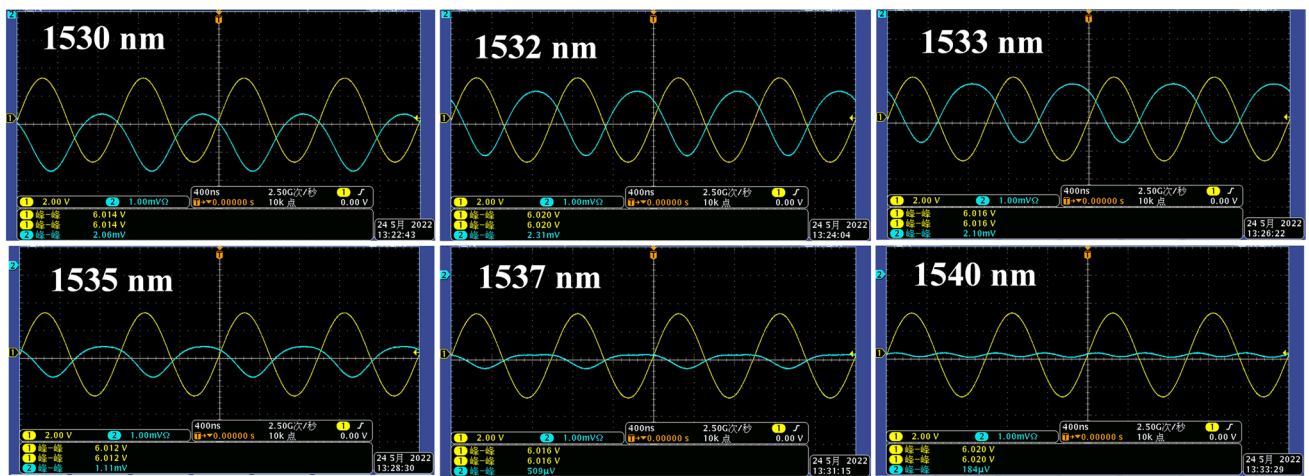


**Fig. 9** Modulation feature achieved with the TMW channel of the packaged GADC754 at different operating wavelength when a 1-MHz and 6-V sinusoidal signal is applied to the tuning electrodes of the GADC

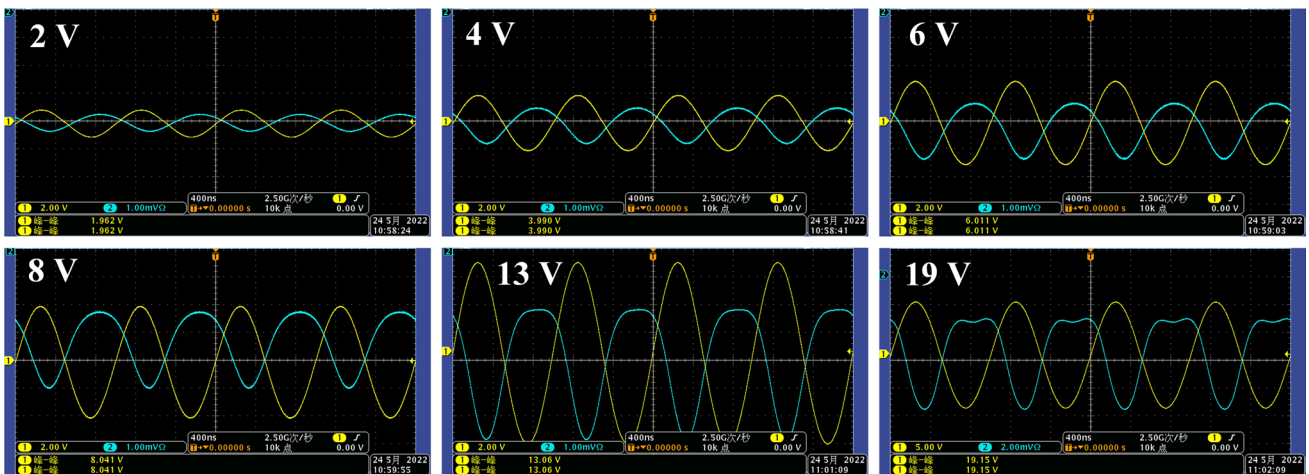


**Fig. 10** Modulation feature achieved with the TMW channel of the packaged GADC754 when the operating wavelength is set at 1533 nm and a 1 MHz sinusoidal signal with different voltage being applied to the tuning electrodes of the GADC

normalized transmission spectra measured at different ambient temperature from 22 to 60 °C are shown in Fig. 11a. Compared with the previous transmission spectrum (see Fig. 7a, 0 V), the transmission spectrum at 22 °C presented in Fig. 11a shows degradations in both isolation and insertion loss. The most possible reason is the degradation of the alignment between the waveguide and the fiber caused by an imperfect butt-joint coupling skill. However, such degradations have no impact on the evaluation of TO tuning of the LN GADC. It can be seen from Fig. 11a that the center wavelength of the rejection band blueshifts from 1533.5 nm to 1528.6 nm when the ambient temperature changes from 22 to 60 °C. The variation of the center wavelength of the rejection band with the change of the ambient temperature, together with the linear fitting lines, is shown in Fig. 11b, indicating a TO tuning efficiency of 0.128 nm/°C.

From Eq. (1),  $\lambda_0$  is determined by  $\Lambda$  and  $\Delta N_{11}$ . During the TO tuning,  $\Lambda$  will be changed by the thermo-expansion effect of LN, while  $\Delta N_{11}$  will be changed mainly by the TO effect of LN. It should be pointed out here that other physical effects of LN, including thermo-expansion effect, photoelastic effect, and pyroelectric effect have also exerted impacts on  $\Delta N_{11}$ ; however, for simplicity and to highlight the impact of TO effect, we can assume reasonably that these other effects have negligible impacts on  $\Delta N_{11}$  during the TO tuning. Next, we investigate qualitatively the change of  $\Delta N_{11}$  caused by the TO effect of LN. It is well known that LN has a positive TO coefficient, which means its refractive index increases with the increase of the ambient temperature. Moreover, according to the fact that a TMW can provide a lower dispersion for the fundamental mode than an SMW, (i.e., the increase of the effective refractive index of the fundamental mode slow down when the width of a waveguide increases), it can be deduced that the increment of  $N_{11T}$  is smaller than that of  $N_{11S}$  when the ambient

temperature increases; hence,  $\Delta N_{11}$  decreases gradually with the increase of the ambient temperature. Considering that the increment of  $\Lambda$  due to the thermo-expansion effect of LN can be negligible, in a low temperature change,  $\lambda_0$  is mainly influenced by  $\Delta N_{11}$ , and with the increase of the ambient temperature  $\Delta N_{11}$  decreases, thus  $\lambda_0$  blueshifts.

## 5 Conclusion

We have demonstrated a high-performance EO tunable GADC in LN based on push–pull electrode. The best one of our fabricated LN GADC by the APE process shows an isolation as high as ~34 dB at the wavelength of 1532.9 nm. We packaged the best LN GADC and investigated its EO tuning and modulation as well as TO tuning characteristics. The experimental results show that our best GADC has two rejection bands, corresponding to the EO tuning ranges of 22.7 nm and 26.1 nm and the EO tuning efficiency of 1.195 nm/V and 1.736 nm/V, respectively. In addition, the measured TO tuning efficiency is 0.128 nm/°C (22–60 °C), respectively. We also investigated the EO modulation characteristics of the TMW channel of the best GADC, and the result shows that it can achieve good EO modulation under the condition of low frequency and small signal. Our proposed GADC could be used as high-speed tunable wavelength filter, mode filter, and EO modulation. It should be pointed out that the size and the performance of our proposed EO tunable GADC can be improved markedly if it was fabricated with the thin-film LN. Nowadays, the thin-film LN has shown its excellent ability in reducing the size and improving the performance of LN-based optical waveguide devices, such as EO mode switch [40], EO modulator [41, 42], polarization beam splitter [43], and so on.

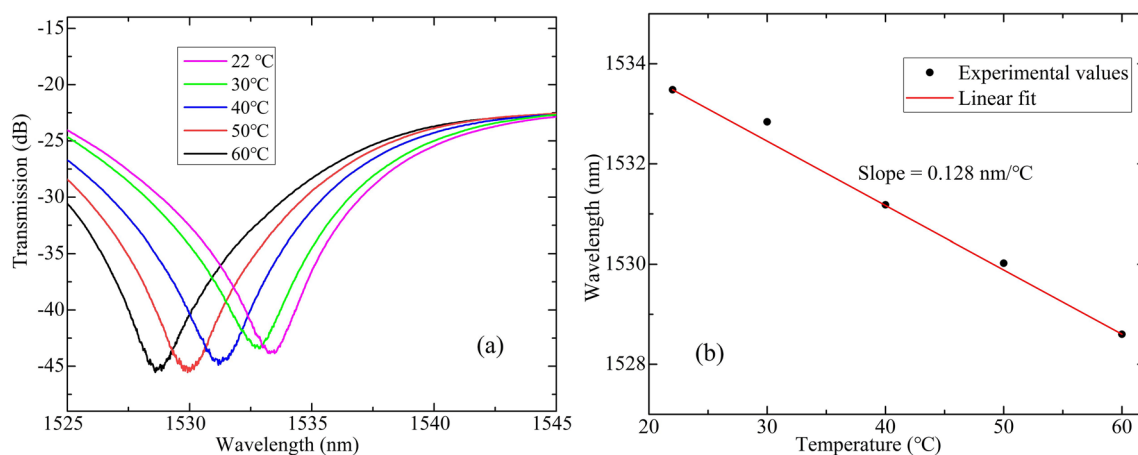


**Fig. 11** **a** Normalized transmission spectra of the TMW of GADC754 measured at different temperature from 22 to 60 °C and **b** variation of the center wavelength with the temperature for the rejection band

**Acknowledgements** This research was supported by the grants from the National Natural Science Foundation of China (NSFC) (Grant Nos. 62075027, U20A20165), the Key R&D Program of Sichuan Province (Grant No. 2020YFSY0003), and the Key Technology R&D Program of Shenzhen (Grant No. JSGG20210802154413040).

**Author contributions** JL and KC wrote the main manuscript text and prepared all figures. Both reviewed the manuscript.

**Data availability** Data underlying the results presented in this paper are not publicly available at this time but may be obtained from the corresponding authors upon reasonable request.

## Declarations

**Conflict of interest** The authors declare no conflict of interest.

## References

- R.R.A. Syms, Optical directional coupler with a grating overlay. *Appl. Opt.* **24**, 717–726 (1985). <https://doi.org/10.1364/AO.24.000717>
- D. Marcuse, Directional couplers made of nonidentical asymmetric slabs part II: grating-assisted couplers. *J. Lightwave Technol.* **5**, 268–273 (1987). <https://doi.org/10.1109/JLT.1987.1075493>
- W. Shi, X. Wang, C. Lin, H. Yun, Y. Liu, T. Baehr-Jones, M. Hochberg, N.A.F. Jaeger, L. Chrostowski, Silicon photonic grating-assisted, contra-directional couplers. *Opt. Exp.* **21**, 3633–3650 (2013). <https://doi.org/10.1364/OE.21.003633>
- M.T. Boroojerdi, M. Ménard, A.G. Kirk, Two-period contra-directional grating assisted coupler. *Opt. Exp.* **24**, 22865–22874 (2016). <https://doi.org/10.1364/OE.24.022865>
- H.Y. Qiu, Y.X. Su, F.Z. Lin, J.F. Jiang, P. Yu, H. Yu, J.Y. Yang, X.Q. Jiang, Silicon add-drop filter based on multimode grating assisted couplers. *IEEE Photon. J.* **8**, 7805308 (2016). <https://doi.org/10.1109/JPHOT.2016.2625268>
- L. Tian, F. Wang, Y.D. Wu, Y.J. Yi, X.Q. Sun, D.M. Zhang, Polymer/silica hybrid integration add-drop filter based on grating-assisted contradirectional coupler. *Opt. Lett.* **43**, 2348–2351 (2018). <https://doi.org/10.1364/OL.43.002348>
- H.Y. Qiu, J.F. Jiang, P. Yu, D.B. Mu, J.Y. Yang, X.Q. Jiang, H. Yu, R. Cheng, L. Chrostowski, Narrow-band add-drop filter based on phase-modulated grating-assisted contra-directional couplers. *J. Lightwave Tech.* **36**, 3760–3764 (2018). <https://doi.org/10.1109/JLT.2018.2852483>
- H.Y. Qiu, J.C. Niu, X. Liang, X.Q. Shen, T. Dai, P. Yu, R. Cheng, Flat-top, sharp-edge add-drop filters using complementary-misalignment-modulated grating-assisted contradirectional couplers. *J. Lightwave Technol.* **39**, 5896–5901 (2021). <https://doi.org/10.1109/JLT.2021.3092045>
- H.Y. Qiu, Y.X. Su, P. Yu, T. Hu, J.Y. Yang, X.Q. Jiang, Compact polarization splitter based on silicon grating-assisted couplers. *Opt. Lett.* **40**, 1885–1887 (2015). <https://doi.org/10.1364/OL.40.001885>
- W. Shi, X. Wang, W. Zhang, H. Yun, C. Lin, L. Chrostowski, N.A.F. Jaeger, Grating-coupled silicon microring resonators. *Appl. Phys. Lett.* **100**, 121118 (2012). <https://doi.org/10.1063/1.3696082>
- J.A. Davis, A. Grieco, M.C.M.M. Souza, N.C. Frateschi, Y. Fainman, Hybrid multimode resonators based on grating-assisted counter-directional couplers. *Opt. Exp.* **25**, 16484–16490 (2017). <https://doi.org/10.1364/OE.25.016484>
- X. Wang, Y. Zhao, Y.H. Ding, S.S. Xiao, J.J. Dong, Tunable optical delay line based on integrated grating-assisted contra-directional couplers. *Photon. Res.* **6**, 880–886 (2018). <https://doi.org/10.1364/PRJ.6.000880>
- L. Zhu, J.Q. Sun, Y. Zhou, Silicon-based wavelength division multiplexer using asymmetric grating-assisted couplers. *Opt. Exp.* **27**, 23234–23248 (2019). <https://doi.org/10.1364/OE.27.023234>
- D.B. Mu, H.Y. Qiu, J.F. Jiang, X.F. Wang, Z.L. Fu, Y.H. Wang, X.Q. Jiang, H. Yu, J.Y. Yang, A four-channel DWDM tunable add/drop demultiplexer based on silicon waveguide Bragg gratings. *IEEE Photon. J.* **11**, 6600708 (2019). <https://doi.org/10.1109/JPHOT.2019.2897359>
- H.Y. Qiu, H. Yu, T. Hu, G.M. Jiang, H.F. Shao, P. Yu, J.Y. Yang, X.Q. Jiang, Silicon mode multi/demultiplexer based on multimode grating-assisted couplers. *Opt. Exp.* **21**, 17904–17911 (2013). <https://doi.org/10.1364/OE.21.017904>
- C.C. Gui, Y. Gao, Z.L. Zhang, J. Wang, On-Chip silicon two-mode (de)multiplexer for OFDM/OQAM data transmission based on grating-assisted coupler. *IEEE Photon. J.* **7**, 7905807 (2015). <https://doi.org/10.1109/JPHOT.2015.2506339>
- X.M. Nie, N.N. Turk, Y. Li, Z.Y. Liu, R. Baets, High extinction ratio on-chip pump-rejection filter based on cascaded grating-assisted contra-directional couplers in silicon nitride rib waveguides. *Opt. Lett.* **44**, 2310–2313 (2019). <https://doi.org/10.1364/OL.44.002310>
- M.S. Kwon, Silicon photonic add-drop filter based on a grating-assisted co-directionally coupled vertical hybrid structure. *Opt. Exp.* **27**, 11748–11765 (2019). <https://doi.org/10.1364/OE.27.011748>
- F. Liu, H. Hier, T.L. Worchesky, Dual-side processed demultiplexer using grating-assisted codirectional coupler. *IEEE Photon. Technol. Lett.* **17**, 600–602 (2005). <https://doi.org/10.1109/LPT.2004.841027>
- R.C. Alferness, T.L. Koch, L.L. Buhl, F. Storz, F. Heismann, M.J.R. Martyak, Grating assisted InGaAsP/InP vertical codirectional coupler filter. *Appl. Phys. Lett.* **55**, 2011–2013 (1989). <https://doi.org/10.1063/1.102148>
- S.W. Ahn, S.Y. Shin, Grating-assisted codirectional coupler filter using electrooptic and passive polymer waveguides. *IEEE J. Sel. Topics Quantum Electron.* **7**, 819–825 (2001). <https://doi.org/10.1109/2944.979343>
- J.H. Li, M.H. Zhou, H. Yao, M.K. Wang, J.Y. Wu, K.X. Chen, Grating-assisted directional coupler in lithium niobate for tunable mode filtering. *IEEE Photon. J.* **13**, 6600807 (2021). <https://doi.org/10.1109/JPHOT.2021.3061089>
- Y. Wang, K. X. Chen, L.F. Wang, K.S. Chiang, Sidewall-grating-assisted polymer-waveguide directional coupler for forward coupling of fundamental modes. *Asia Commun. Photon. Conf. ASu3A.3* (2015). <https://doi.org/10.1364/ACPC.2015.ASu3A.3>
- Q. Liu, Z.H. Gu, M.K. Park, J.H. Chung, Experimental demonstration of highly sensitive optical sensor based on grating-assisted light coupling between strip and slot waveguides. *Opt. Exp.* **24**, 12549–12556 (2016). <https://doi.org/10.1364/OE.24.012549>
- F.W. Dabby, A. Kestenbaum, U.C. Paek, Periodic dielectric waveguides. *Opt. Commun.* **6**, 125–130 (1972). [https://doi.org/10.1016/0030-4018\(72\)90209-X](https://doi.org/10.1016/0030-4018(72)90209-X)
- K. Sukada, A. Yariv, Analysis of optical propagation in a corrugated dielectric waveguide. *Opt. Commun.* **8**, 1–4 (1973). [https://doi.org/10.1016/0030-4018\(73\)90167-3](https://doi.org/10.1016/0030-4018(73)90167-3)
- A. Yariv, M. Nakamura, Periodic structures for integrated optics. *IEEE J. Quantum Electron.* **13**, 233–252 (1977). <https://doi.org/10.1109/JQE.1977.1069323>
- R.V. Schmidt, D.C. Flanders, C.V. Shank, R.D. Standley, Narrow-band grating filters for thin-film optical waveguides. *Appl. Phys. Lett.* **25**, 651–652 (1974). <https://doi.org/10.1063/1.1655346>

29. J. Bjorkholm, C. Shank, Distributed feedback lasers in thin film optical waveguides. *IEEE J. Quantum Electron.* **8**, 833–838 (1972). <https://doi.org/10.1109/JQE.1972.1076871>
30. Y.P. Wang, J.P. Cheng, X.W. Li, J.H. Zhou, H. Shen, C.H. Shi, X.H. Zhang, J.X. Hong, A.L. Ye, Fast tunable electro-optic polymer waveguide gratings. *Acta Phys. Sin.* **54**, 4782–4788 (2005)
31. W.F. Zhang, N. Ehteshami, W.L. Liu, J.P. Yao, Silicon-based on-chip electrically tunable sidewall Bragg grating Fabry-Perot filter. *Opt. Lett.* **40**, 3153–3156 (2015). <https://doi.org/10.1364/OL.40.003153>
32. K. Abdelsalam, E. Ordouie, M.G. Vazimali, F.A. Juneghani, P. Kumar, G.S. Kanter, S. Fathpour, Tunable dual-channel ultranarrowband Bragg grating filter on thin-film lithium niobate. *Opt. Lett.* **46**, 2730–2733 (2021). <https://doi.org/10.1364/OL.427101>
33. A. D'Alessandro, D. Donisi, L.D. Sio, R. Beccherelli, R. Asquini, R. Caputo, C. Umerton, Tunable integrated optical filter made of a glass ion-exchanged waveguide and an electro-optic composite holographic grating. *Opt. Exp.* **16**, 9254–9260 (2008). <https://doi.org/10.1364/OE.16.009254>
34. A. Paliwal, A. Sharma, R. Guo, A.S. Bhalla, V. Gupta, M. Tomar, Electro-optic (EO) effect in proton-exchanged lithium niobate: towards EO modulator. *Appl. Phys. B.* **125**, 115 (2019). <https://doi.org/10.1007/s00340-019-7227-7>
35. M. Bazzan, C. Sada, Optical waveguides in lithium niobate: Recent developments and applications. *Appl. Phys. Rev.* **2**, 040603 (2015). <https://doi.org/10.1063/1.4931601>
36. M.R. Zhang, W. Ai, K.X. Chen, W. Jin, K.S. Chiang, A lithium-niobate waveguide directional coupler for switchable mode multiplexing. *IEEE Photon. Technol. Lett.* **30**, 1764–1767 (2018). <https://doi.org/10.1109/LPT.2018.2868834>
37. M.R. Zhang, K.X. Chen, W. Jin, J.Y. Wu, K.S. Chiang, Electro-optic mode-selective switch based on cascaded three-dimensional lithium-niobate waveguide directional couplers. *Opt. Exp.* **28**, 35506–35517 (2020). <https://doi.org/10.1364/OE.406020>
38. K.S. Chiang, S.Y. Cheng, Technique of applying the prism-coupler method for accurate measurement of the effective indices of channel waveguides. *Opt. Eng.* **47**, 034601 (2008). <https://doi.org/10.1117/1.2896412>
39. Q. Liu, K.S. Chiang, V. Rastogi, Analysis of corrugated long-period gratings in slab waveguides and their polarization dependence. *J. Lightwave Tech.* **21**, 3399–3405 (2003). <https://doi.org/10.1109/JLT.2003.821749>
40. Y.H. Jiang, X. Han, Y.Y. Li, H.F. Xiao, H.J. Huang, P. Zhang, A. Dubey, M.R. Yuan, T.G. Nguyen, A. Boes, Y.T. Li, G.H. Ren, J.Z. Xue, Q.F. Hao, Y.K. Su, A. Mitchell, Y.H. Tian, High-speed optical mode switch in lithium niobate on insulator. *ACS Photon.* (2023). <https://doi.org/10.1021/acsp Photonics.2c01364>
41. M.K. Wang, J.H. Li, H. Yao, X.P. Li, J.Y. Wu, K.S. Chiang, K.X. Chen, Thin-film lithium-niobate modulator with a combined passive bias and thermo-optic bias. *Opt. Exp.* **30**, 39706–39715 (2022). <https://doi.org/10.1364/OE.474594>
42. M.Y. Xu, Y.T. Zhu, F. Pittalà, J. Tang, M.B. He, W.C. Ng, J.Y. Wang, Z.L. Ruan, X.F. Tang, M. Kuschnerov, L. Liu, S.Y. Yu, B.F. Zheng, X.L. Cai, Dual-polarization thin-film lithium niobate in-phase quadrature modulators for terabit-per-second transmission. *Optica.* **9**, 61–62 (2022). <https://doi.org/10.1364/OPTICA.449691>
43. H.N. Xu, D.X. Dai, L. Liu, Y.C. Shi, Proposal for an ultra-broadband polarization beam splitter using an anisotropy-engineered Mach-Zehnder interferometer on the x-cut lithium-niobate-on-insulator. *Opt. Exp.* **28**, 10899–10908 (2020). <https://doi.org/10.1364/OE.390075>

**Publisher's Note** Springer Nature remains neutral with regard to jurisdictional claims in published maps and institutional affiliations.

Springer Nature or its licensor (e.g. a society or other partner) holds exclusive rights to this article under a publishing agreement with the author(s) or other rightsholder(s); author self-archiving of the accepted manuscript version of this article is solely governed by the terms of such publishing agreement and applicable law.